Magnetic Resonance Imaging 62 (2019) 181–190

Contents lists available at ScienceDirect

Magnetic Resonance Imaging

journal homepage: www.elsevier.com/locate/mri

Original contribution

Amide proton transfer imaging of glioblastoma, neuroblastoma, and breast cancer cells on a 11.7 T magnetic resonance imaging system

Minori Tanoue[a,b], Shigeyoshi Saito[c,*], Yusuke Takahashi[d], Rikita Araki[e], Takashi Hashido[c], Hidetaka Kioka[d], Yasushi Sakata[d], Yoshichika Yoshioka[a,b]

[a] Laboratory of Biofunctional Imaging, Graduate School of Frontier Biosciences, Osaka University, Suita, Osaka 560-0871, Japan
[b] Institute for Open and Transdisciplinary Research Initiatives, Osaka University, Suita, Osaka 560-0871, Japan
[c] Department of Medical Physics and Engineering, Division of Health Sciences, Osaka University Graduate School of Medicine, Suita, Osaka 560-0871, Japan
[d] Department of Cardiovascular Medicine, Osaka University Graduate School of Medicine, Suita, Osaka 565-0871, Japan
[e] BioSpin Division, Bruker Japan K.K., Yokohama, Kanagawa 221-0022, Japan

ARTICLE INFO

Keywords:
Chemical exchange saturation transfer
Magnetic resonance imaging
Glioma
Amide proton imaging

ABSTRACT

Purpose: The purpose of this study was (i) to determine the optimal magnetization transfer (MT) pulse parameter for amide proton transfer (APT) chemical exchange saturation transfer (CEST) imaging on an ultra-high-field magnetic resonance imaging (MRI) system and (ii) to use APT CEST imaging to noninvasively assess brain orthotopic and ectopic tumor cells transplanted into the mouse brain.

Methods: To evaluate APT without the influence of other metabolites, we prepared egg white phantoms. Next, we used 7–11-week-old nude female mice and the following cell lines to establish tumors after injection into the left striatum of mice: C6 (rat glioma, n = 8) as primary tumors and Neuro-2A (mouse neuroblastoma, n = 11) and MDA-MB231 (human breast cancer, n = 8) as metastatic tumors. All MRI experiments were performed on an 11.7 T vertical-bore scanner. CEST imaging was performed at 1 week after injection of Neuro-2A cells and at 2 weeks after injection of C6 and MDA-MB231 cells. The MT pulse amplitude was set at 2.2 μT or 4.4 μT. We calculated and compared the magnetization transfer ratio (MTR) and difference of MTR asymmetry between normal tissue and tumor (ΔMTR asymmetry) on APT CEST images between mouse models of brain tumors. Then, we performed hematoxylin and eosin (HE) staining and Ki-67 immunohistochemical staining to compare the APT CEST effect on tumor tissues and the pathological findings.

Results: Phantom study of the amide proton phantom containing chicken egg white, z-spectra obtained at a pulse length of 500 ms showed smaller peaks, whereas those obtained at a pulse length of 2000 ms showed slightly higher peaks. The APT CEST effect on tumor tissues was clearer at a pulse amplitude of 2.2 μT than at 4.4 μT. For all mouse models of brain tumors, ΔMTR asymmetry was higher at 2.2 μT than at 4.4 μT. ΔMTR asymmetry was significantly higher for the Neuro-2A model than for the MDA-MB231 model. HE staining revealed light bleeding in Neuro-2A tumors. Immunohistochemical staining revealed that the density of Ki-67-positive cells was higher in Neuro-2A tumors than in C6 or MDA-MB231 tumors.

Conclusion: The MTR was higher at 4.4 μT than at 2.2 μT for each concentration of egg white at a pulse length of 500 ms or 2000 ms. High-resolution APT CEST imaging on an ultra-high-field MRI system was able to provide tumor information such as proliferative potential and intratumoral bleeding, noninvasively.

Abbreviations: ADC, apparent diffusion coefficient; APT, amide proton transfer; AREX, apparent exchange-dependent relaxation; CEST, chemical exchange saturation transfer; FASTMAP, fast automatic shimming technique by mapping along projections; FBS, fetal bovine serum; FLAIR, fluid attenuated inversion recovery; DMEM, Dulbecco's modified Eagle's medium; DWI, diffusion-weighted imaging; HE, hematoxylin and eosin; MTR, magnetization transfer ratio; MT, magnetization transfer; MRI, magnetic resonance imaging; MRS, magnetic resonance spectroscopy; NOE, nuclear Overhauser effect; PFA, paraformaldehyde; PS, penicillin-streptomycin; RARE, rapid acquisition with relaxation enhancement; rCBV, relative cerebral blood volume; RF, radio frequency; T_1WI, T_1-weighted image; T_2WI, T_2-weighted image; TurboRARE, turbo rapid acquisition with relaxation enhancement; WASABI, water shift and B1; WASSR, water saturation shift referencing

* Corresponding author.
E-mail address: saito@sahs.med.osaka-u.ac.jp (S. Saito).

https://doi.org/10.1016/j.mri.2019.07.005
Received 12 February 2019; Received in revised form 10 July 2019; Accepted 10 July 2019
0730-725X/ © 2019 Elsevier Inc. All rights reserved.

1. Introduction

1.1. Noninvasive molecular imaging: the recent development of chemical exchange saturation transfer (CEST)

Magnetic resonance imaging (MRI) is a noninvasive medical imaging technique that produces detailed images of internal structures of the body. While MRI provides anatomical information, magnetic resonance spectroscopy (MRS) enables in vivo assessment of the chemical composition of tissues by measuring signals from chemical compounds such as brain metabolites. CEST is a recent contrast enhancement technique that enables the indirect detection of molecules with exchangeable protons and exchange-related properties [1]. These protons can be selectively saturated by a radio-frequency (RF) pulse, also called magnetization transfer (MT) pulse, and can be exchanged with unsaturated protons in a static magnetic field. Using this process, low concentrations of molecules can be detected. CEST imaging can be classified into two types: exogenous and endogenous. Exogenous CEST agents employ a class of diamagnetic molecules that contain exchangeable NH or OH protons [2]. Typical endogenous CEST agents are amide protons (from peptides and proteins), amine protons (from glutamate and creatine), and hydroxyl protons (from glycosaminoglycan, myo-inositol, and lactate) [3,4].

In CEST imaging, various MR parameters and physiological factors influence the level of the CEST effect (e.g., magnetic strength, RF magnitude, B_0 and B_1 homogeneity, tissue relaxation rate, CEST agent concentration, pH, and temperature) [1]. There are many biological sources of CEST signals (e.g., the brain) [5]. Therefore, it is important to suit the parameters to detect the target chemical molecule (e.g., a brain metabolite) with high sensitivity. Ultra-high-field MRI presents various benefits, such as higher signal-to-noise ratio, greater CEST effect, higher chemical shift, and longer T_1 relaxation time of water [1,2]. However, there are some technical problems related to CEST imaging using ultra-high-field MRI (e.g., 11.7 T MRI), such as the magnetic field inhomogeneity presented in ultra-high-field MRI. Problems associated with poor magnet homogeneity include spatial distortion, blurring, intensity loss, curved slice profiles, and banding artifacts. In addition, field homogeneity is the most important factor in high-quality CEST imaging.

1.2. Imaging techniques for brain tumors

Tumor grading is important to treatment planning and prognosis prediction. For instance, gliomas can be graded from 1 to 4 according to their degree of malignancy [6]. In clinical practice, MRI is essential to understand a tumor lesion's site and malignancy. During MRI examination, T_1-weighted images (T_1WI), T_2-weighted images (T_2WI), and fluid-attenuated inversion recovery (FLAIR) sequences can be used to evaluate a brain tumor. Contrast images from diffusion-weighted imaging (DWI), perfusion MRI, and MRS can provide additional information. On T_1WI with the gadolinium contrast agent, high-grade gliomas and metastases show ring enhancement surrounding a central area of necrosis [7]. Advanced MRI metrics, such as DWI apparent diffusion coefficient (ADC) and perfusion MRI relative cerebral blood value (rCBV), can distinguish between high-grade and low-grade gliomas [8]. In most cases, metastatic brain tumors can be distinguished from primary brain tumors by the number, location, and structure of lesions visualized by conventional MRI examination [7]. However, it is difficult to distinguish between metastatic and primary brain tumor subtypes by perfusion MRI, DWI, and MRS [8].

1.3. Amide proton transfer (APT) CEST imaging

APT CEST imaging has attracted attention as a new tool to grade brain tumor malignancy. APT CEST can differentiate tumors from normal tissue by the increased concentration of mobile peptides and proteins in the former [9]. APT correlates with brain tumor grade [3,10], and APT CEST imaging has been suggested to be more useful than ADC and rCBV in malignancy diagnosis such as tumor grading [11]. Therefore, APT CEST imaging may be useful in the diagnosis of various brain diseases as well as in differential diagnosis [12–14]. However, it is not known whether primary and metastatic brain tumors can be distinguished by using APT CEST imaging, which may be a useful alternative to perfusion MRI, DWI, MRS [11]. In mice, APT CEST imaging has been used to study xenograft and allograft brain tumors [15].

1.4. Purpose of this study

The purpose of this study was (i) to determine the suitable MT pulse parameter for APT CEST imaging on an ultra-high-field MRI system; and (ii) to use APT CEST imaging to noninvasively assess three types of tumor cells transplanted into the mouse brain.

2. Materials and methods

2.1. Preparation of phantoms for imaging studies

To evaluate APT without the influence of other metabolites, we prepared egg white phantoms. Chicken eggs were commercially obtained. We prepared phantoms containing 20%, 50%, or 100% of egg white in phosphate-buffered saline (PBS; Wako, Osaka, Japan).

2.2. MRI of egg white phantoms

All MRI experiments were performed on an 11.7 T vertical-bore scanner (Bruker Avance II; Bruker BioSpin, Ettlingen, Germany) equipped with a custom-made transmit/receive volume RF coil with a diameter of 25 mm (m2 m Imaging Corp., Cleveland, OH, USA), using the ParaVision 6.0 console system (Bruker BioSpin). For B_0 shimming, first-order shimming for the selected volume was conducted using the fast automatic shimming technique by mapping along projections (FASTMAP) algorithm. B_1 and B_0 maps were calculated point-by-point for each correction using a method referred to as the "180° signal null" [16] and water saturation shift referencing (WASSR) [17]. Single-slice multiple MT MRI was performed using the rapid acquisition with relaxation enhancement (RARE) sequence for CEST imaging with the following parameters: repetition time = 4500 ms; echo time = 4.62 ms; RARE factor = 10; number of average = 1; field of view = 24 × 24 mm^2; matrix size = 64 × 64; and slice thickness = 1.0 mm. Z-spectrum data were acquired from 19 CEST images with varying saturation frequencies from −4.8 ppm to +4.8 ppm in 0.6-ppm steps. S_0 images (without saturation RF pulses) were acquired before CEST images. To fit the saturation RF pulse parameter (i.e., MT pulse), CEST imaging was performed under four conditions, as follows: length = 49.99 ms; interpulse delay = 0.01 ms; number of pulses = 10 or 40 (pulse length = 500 ms or 2000 ms); and amplitude = 2.2 μT or 4.4 μT; pulse shape = block pulse.

2.3. Cell culture

C6 rat glioma, Neuro-2A mouse neuroblastoma, and MDA-MB231 human breast cancer cells were purchased from JCRB Cell Bank (National Institutes of Biomedical Innovation, Health and Nutrition, Osaka, Japan). We cultured the cells in Dulbecco's modified Eagle's medium (DMEM) supplemented with 10% fetal bovine serum (FBS) and 1% penicillin-streptomycin (PS) solution at 37 °C with 5% CO_2.

2.4. Animal experiments

All experimental protocols were approved by the Research Ethics Committee of our University. All experimental procedures involving

animals and their care were carried out in accordance with the Osaka University Guidelines for Animal Experimentation and the National Institutes of Health Guide for the Care and Use of Laboratory Animals. Animal experiments were performed in twenty-seven 7- to 11-week-old (16–24 g, C6: n = 8, Neuro-2A: n = 11, MDA-MB231: n = 8) female BALB/c nu/nu mice purchased from Japan SLC (Hamamatsu, Japan). All mice were housed in a controlled vivarium environment (24 °C; 12:12 h light:dark cycle) and fed a standard pellet diet and water ad libitum. To inject the tumor cells, we first anesthetized the mice with a mixture of air and 4% isoflurane (Wako Pure Chemical Industries, Ltd., Osaka, Japan). To perform the operation, we immobilized the mice using a brain retainer (Stereotaxic Instruments for Rats, NARISHIGE SCIENTIFIC INSTRUMENT LAB, Tokyo, Japan). During the operation, the mice were continuously anesthetized with 2% isoflurane. The left skull was drilled (2 mm lateral and 1 mm anterior to bregma) using an electric drill. Then, $1.0 \times 10^5/2$ μL C6, Neuro-2A, or MDA-MB231 cells were injected 2 mm deep to the surface of the skull at an injection rate of 0.5 μL/min using 26-gauge needles.

2.5. MRI of mice

In vivo MRI experiments were performed using MRI, equipped with a transmit/receive volume RF coil with a diameter of 20 mm (m2 m Imaging Corp.), as in the phantom study. Axial T_2WI were acquired around the mouse brain using the turbo rapid acquisition with relaxation enhancement (TurboRARE) sequence with the following parameters: repetition time = 4000 ms; echo time = 40 ms; RARE factor = 8; number of average = 4; field of view = 19.6 × 19.6 mm^2; matrix size = 256 × 256; and slice thickness = 0.5 mm. CEST image slices were obtained at the region of maximum tumor width. For B_0 shimming, first-order shimming for the selected volume was conducted using the FASTMAP algorithm. Single-slice multiple MT MRI was performed using RARE for CEST imaging with the following parameters: repetition time = 4500 ms; echo time = 4.62 ms; RARE factor = 10; number of average = 1; field of view = 16 × 16 mm^2; matrix size = 64 × 64; and slice thickness = 0.5 mm. Z-spectrum data were acquired from CEST images with varying saturation frequencies from −4.2 ppm to +4.2 ppm in 0.6-ppm steps. S_0 images (without saturation RF pulses) were acquired before CEST images. To fite the MT pulse parameter, CEST imaging was performed under four conditions as follows: length = 49.99 ms; interpulse delay = 0.01 ms; number of pulses = 10 (for C6 only) or 40 (pulse length = 500 ms or 2000 ms); amplitude = 2.2 μT or 4.4 μT; pulse shape = block pulse [18]. The total acquisition time per animal was approximately 70 min.

2.6. Calculation of the MTR

We calculated the MTR asymmetry using the following equation: $MTR_{asym}(\%) = (S_{[-\alpha ppm]} - S_{[+\alpha ppm]})/S_0$. APT CEST signal was defined as an MTR asymmetry of +3.6 ppm. The region of interest (ROI) of normal tissue was set on the MTR map (ROI size = 3.4 ± 1.1 mm^2). MTR asymmetry was expressed as mean ± standard deviation (SD). The ROI of normal tissue was set as a homogeneous area such as normal-appearing brain near the implantation site for comparison with the tumor tissue. The ΔMTR asymmetry was defined as follows: $\Delta MTR_{asym}(\%) = (MTR_{tumor} - MTR_{normal})$. All calculations and analyses were performed using MATLAB (MathWorks, Natick, MA, USA) [5,19].

2.7. Histological studies

We used hematoxylin and eosin (HE) staining to observe the tissue morphology. In addition, we used Ki-67 immunohistochemical staining to evaluate tumor cell proliferation. After MRI, the brain was harvested and fixed over one day in 4% paraformaldehyde (PFA). Then, the brain was embedded in paraffin wax. Tissue sections were cut with a microtome at a thickness of 5 μm. The sections were dewaxed in xylene and rehydrated by a series of ethanol-water washes. After washing in purified water for 5 min, the sections were incubated for 5 min with hematoxylin and rinsed twice in purified water for 5 min. Next, the sections were incubated for 3 min with eosin and rinsed in purified water for approximately 30 s. Then, the sections were rehydrated by a series of ethanol-water washes and dewaxed in xylene. Finally, the slides were mounted.

For Ki-67 immunohistochemical staining, after washing three times in purified water for 5 min, the sections were pre-treated using heat-mediated antigen retrieval with sodium citrate buffer (pH 6.0) at 125 °C for 10 min. After cooling to room temperature, the sections were washed thoroughly with purified water. Then, they were incubated with 3% H_2O_2 in purified water for 30 min and washed in 0.025% Triton X-100 in PBS (PBST) with gentle agitation. Next, they were blocked in 10% normal goat serum in PBST for 1 h at room temperature. After removing the blocking solution, they were incubated with anti-Ki-67 antibody (2 μg/mL, ab15580; Abcam, Cambridge, UK) overnight at 5 °C. On the next day, they were rinsed in PBST and incubated with anti-rabbit immunoglobulin G (IgG) biotinylated antibody for 1 h at room temperature. After rinsing in PBST, the avidin–biotinylated enzyme complex was applied for 30 min at room temperature (VECTASTAIN® ABC kits, VECTOR Laboratories, Inc., CA, USA). After rinsing again in PBST, diamino benzidine (DAB) was applied for 10 min. The sections were then washed thoroughly in purified water, dehydrated through a series of ethanol-water washes, and dewaxed in xylene. Thereafter, the slides were mounted. All sections were imaged under a Keyence BZ-X710 All-in-One fluorescence microscope (KEYENCE, Osaka, Japan) after staining for histological analysis. Ki-67 (for the assessment of tumor proliferation) was identified as follows. 1) The brightness and contrast were automatically optimized using Photoshop (Ver. 8.0.1, Adobe, Inc., CA, USA). 2) The brown-stained positive cells were enhanced and converted to a black-and-white binary map using the “Make binary” plug-in of ImageJ (Ver.1.51j8, National Institute of Health, MA, USA). 3) The total area of the black regions of the binary map was measured using the “ROI” “Measure” plug-ins of ImageJ. 4) The ratio of the positive-cell area to the total area was calculated [20].

2.8. Statistical analysis

The estimated parameter values were expressed as the mean ± SD. Differences in MTR asymmetry among groups were analyzed by two-way analysis of variance using Prism 5 (Version 5, GraphPad Software, CA, USA). Statistical significance was determined by Bonferroni's multiple comparison test. A p-value < 0.05 was considered statistically significant.

3. Results

Fig. 1 shows the MRI images of the amide proton phantom containing chicken egg white. In Fig. 1A, a T_2WI shows the position of the phantoms. Fig. 1B–E show APT CEST images of the egg white phantoms under various conditions of MT pulse. The APT CEST images revealed that the contrast depended on the concentration of egg white and the MT pulse condition. Fig. 2 shows the Z-spectra obtained under various conditions of MT pulse. The peaks were observed at around +3.6 ppm, where the signal of APT was obtained. Z-spectra obtained at an amplitude of 2.2 μT showed smaller peaks (Fig. 2A, C), whereas those obtained at an amplitude of 4.4 μT showed higher peaks (Fig. 2B, D). Z-spectra obtained at a pulse length of 500 ms showed smaller peaks (Fig. 2A, B), whereas those obtained at a pulse length of 2000 ms showed higher peaks (Fig. 2C, D).

Fig. 3 shows the relationship between the concentration of egg white and MTR asymmetry at +3.6 ppm. The MTR asymmetry at +3.6 ppm was higher in the 100% egg white phantom than in the 20% egg white phantom. The MTR asymmetry was higher at 4.4 μT than at 2.2 μT for each concentration of egg white at a pulse length of 500 ms

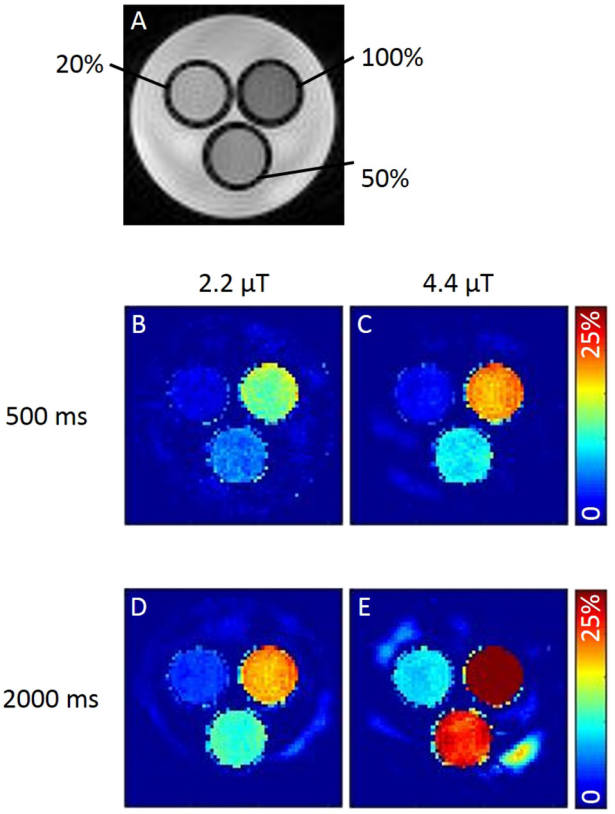

Fig. 1. Images of the amide proton phantoms containing chicken egg white. A: A T_2-weighted image showing the position of the phantoms. B–E: Amide proton transfer images at +3.6 ppm obtained using various conditions of magnetization transfer pulse (B: amplitude = 2.2 μT, pulse length = 500 ms; C: amplitude = 4.4 μT, pulse length = 500 ms; D: amplitude = 2.2 μT, pulse length = 2000 ms; and E: amplitude = 4.4 μT, pulse length = 2000 ms).

(Fig. 3A) or 2000 ms (Fig. 3B).

Fig. 4 shows axial T_2WI and APT maps slices of the mouse brain obtained 2 weeks after the injection of C6 glioma tumor cells. In the T_2WI, the signal intensities of the tumor and the brain tissue were similar (Fig. 4A). A clearer region of high APT signal consistent with tumor tissue was obtained at a pulse length of 500 ms or 2000 ms (Fig. 4B–E). Fig. 5A–D shows the MTR asymmetry in the region of the tumor or normal tissue and the ΔMTR asymmetry between tumor and normal tissue. At approximately +3.6 ppm, the ΔMTR asymmetry was increased. In particular, at a pulse length of 2000 ms and an amplitude of 2.2 μT, the ΔMTR asymmetry reached its maximum value at +3.6 ppm (Fig. 5A). Fig. 6 shows the ΔMTR asymmetry at +3.6 ppm obtained under various conditions of MT pulse. The ΔMTR asymmetry was significantly higher at a pulse length of 2000 ms and an amplitude of 2.2 μT than in the other conditions (p-value < 0.05).

Fig. 7 shows axial images of C6, Neuro-2A, and MDA-MB231 tumors grown in the mouse brain. In T_2WI of C6- or MDA-MB231-injected mice, the tumor tissue showed a signal intensity comparable to the normal tissue (Fig. 7A, G). In all Neuro-2A-injected mice, the tumor tissue showed a low signal (n = 8, Fig. 7D). These mice showed bleeding in the tumor, confirmed by HE staining, while no animal in the C6 and the MDA-MB231 group showed bleeding. Fig. 7B, E, and H show APT maps obtained at a pulse amplitude of 2.2 μT. Fig. 7C, F, and I show APT maps obtained at a pulse amplitude of 4.4 μT. When the amplitude of the MT pulse was 2.2 μT, a clearer region of high APT signal consistent with tumor tissue was obtained (Fig. 7B, E, H). Fig. 8 shows ΔMTR asymmetry at +3.6 ppm. There was no difference in the ΔMTR asymmetry between mouse models of brain tumors in images obtained at a pulse amplitude of 2.2 μT (Fig. 8A). In images obtained at a pulse amplitude of 4.4 μT, the ΔMTR_{asym} was significantly higher for Neuro-2A tumors than for MDA-MB231 tumors (Fig. 8B, p value < 0.05).

Fig. 9 shows histological sections of tumor tissue (Fig. 9A, C, E: HE staining; Fig. 9B, D, F: Ki-67 immunohistochemical staining). In Neuro-2A tumors, intratumoral bleeding was observed (Fig. 9C). The density of Ki-67-positive cells in tumors is shown in Fig. 10. The density of Ki-

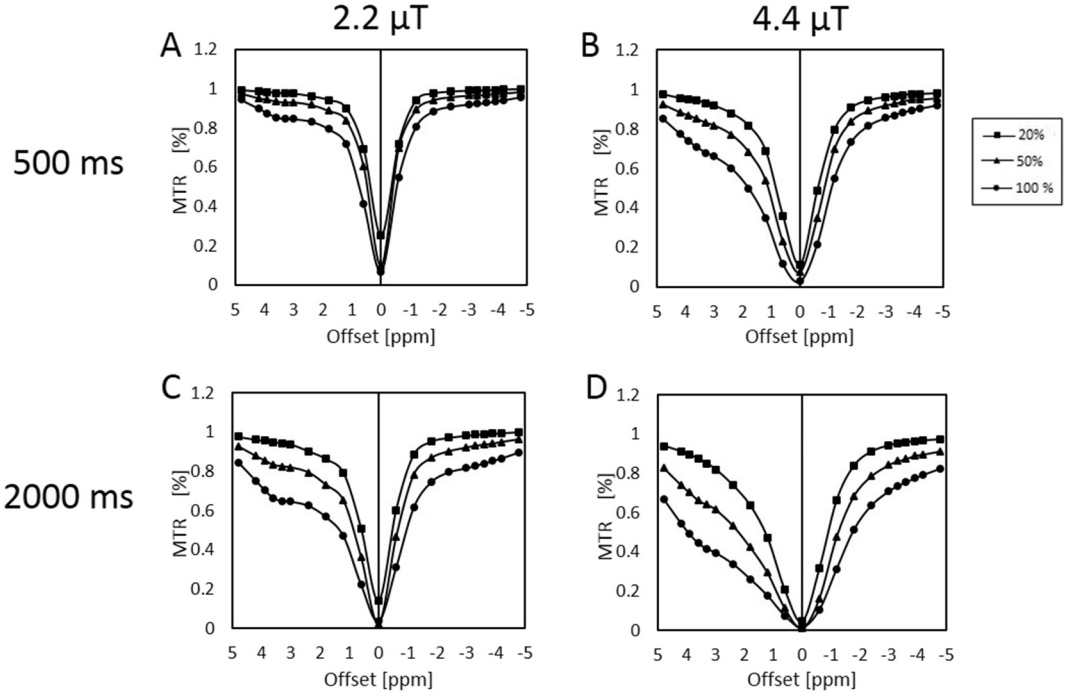

Fig. 2. Z-spectra of 20%, 50%, and 100% egg white phantoms at various conditions of saturation radio frequency pulse (A: amplitude = 2.2 μT, pulse length = 500 ms; B: amplitude = 4.4 μT, pulse length = 500 ms; C: amplitude = 2.2 μT, pulse length = 2000 ms; and D: amplitude = 4.4 μT, pulse length = 2000 ms). MTR = magnetization transfer ratio.

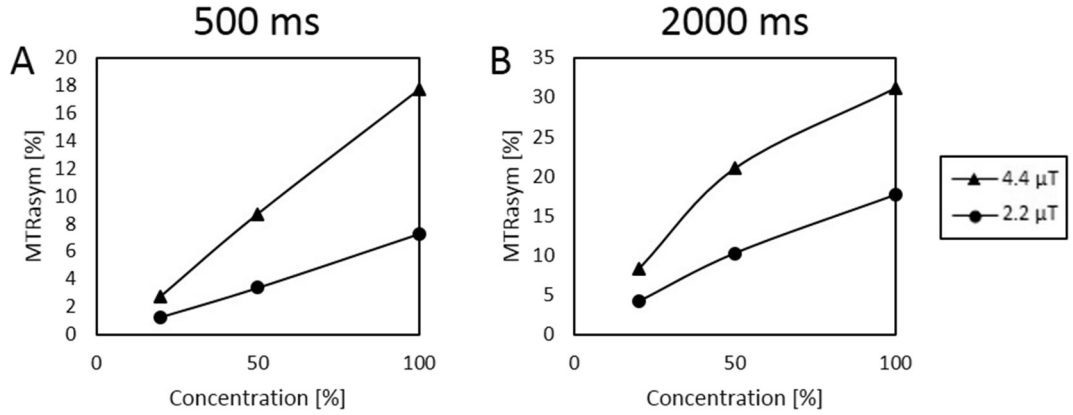

Fig. 3. Magnetization transfer ratio asymmetry (MTR_{asym}) (%) at various conditions of saturation radio frequency pulse at +3.6 ppm (A: pulse length = 500 ms; and B: pulse length = 2000 ms).

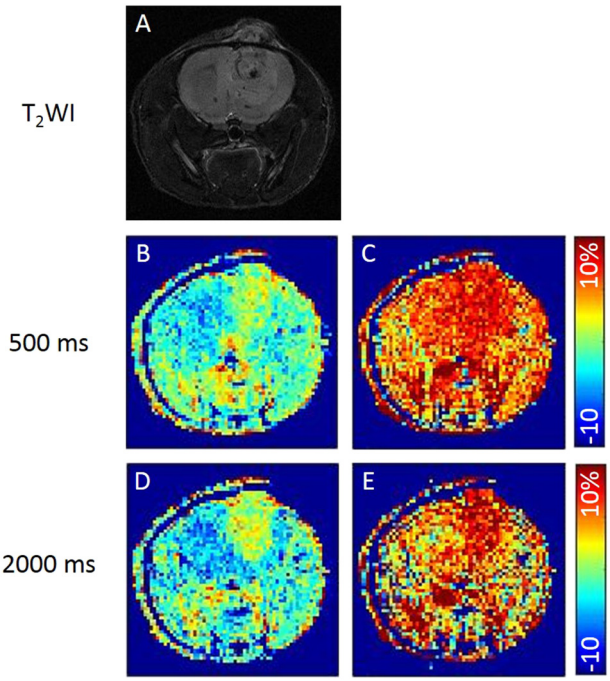

Fig. 4. Typical images of a brain tumor derived from C6 cells at 2 weeks after injection into a mouse. A: A T_2-weighted image (T_2WI). B–E: Amide proton transfer images at +3.6 ppm obtained using various conditions of magnetization transfer pulse (B: amplitude = 2.2 μT, pulse length = 500 ms; C: amplitude = 4.4 μT, pulse length = 500 ms; D: amplitude = 2.2 μT, pulse length = 2000 ms; and E: amplitude = 4.4 μT, pulse length = 2000 ms).

67-positive cells was significantly higher in Neuro-2A tumors than in C6 or MDA-MB231 tumors (p-value < 0.05). This finding was similar to the pattern observed for ΔMTR asymmetry. Fig. 11 shows an APT CEST image and an HE-stained image of a Neuro-2A tumor. The region of intratumoral bleeding showed the highest APT signal intensity.

4. Discussion

This study determined the suitable parameter of MT pulse for APT CEST imaging using an egg white phantom and brain tumor models. APT maps of phantoms revealed that the contrast depended on the concentration of egg white. The difference in MTR asymmetry between tumor and normal tissue in mice with C6 tumors was higher at 2000 ms of pulse length and 2.2 μT of amplitude than under other conditions. The APT CEST effect in brain tumors reflects not only the proliferative potential of each tumor but also intratumoral bleeding.

4.1. APT signals and correlation with tumors

A longer length of MT pulse enhances the CEST effect because it builds up or maintains the saturation of exchangeable protons and enables more accumulation of exchanged protons in bulk water [21,22]. In addition, the MT effect of exchangeable protons increases gradually with a higher amplitude of saturation pulse. However, the MT effect reaches its maximum value at a suitable amplitude and then is reduced at higher amplitudes due to “spillover” effects caused by a direct MT between water and protons [23]. The NOE of aliphatic protons, the transfer of nuclear spin polarization from one nuclear spin population to another via cross-relaxation, should also be kept in mind in APT imaging on an 11.7 T high-field MRI system [24]. The NOE signal is detected around −3.5 ppm, a position that is symmetrical to the APT signals. The NOE signal is clearly visible at a lower amplitude of MT pulse and is lower in tumors than in normal tissue [24–26]. Therefore, the decrease in NOE signal in tumors is due to an increase in the APT signal at 2.2 μT of amplitude using MTR asymmetry at +3.6 ppm. A longer length of MT pulse is suitable for APT CEST imaging because it enhances the CEST effect. Our findings suggest that the ΔMTR asymmetry at +3.6 ppm reflected an increase in APT signal and a decrease in NOE signal at a lower amplitude of saturation pulse.

APT maps of mouse brains growing tumors derived from three different tumor cell lines were examined to evaluate which features affect APT signals. In our study, the ΔMTR asymmetry was significantly higher in Neuro-2A tumors than in MDA-MB231 tumors. Ki-67 immunohistochemical staining revealed that the proliferative potential of tumor cells was significantly higher in Neuro-2A tumors than in C6 or MDA-MB231 tumors. Neuro-2A is a mouse neural crest-derived cell line that has been extensively used to study neuronal differentiation, axonal growth and signaling pathways. A large number of Neuro-2A cells proliferate under standard culture conditions, and these cells can differentiate into specific neural cells, such as dopaminergic neurons or neurons possessing dendrite-like processes, under specific conditions [27,28]. Neuro-2A showed high potential to proliferate. Further, HE staining showed intratumoral bleeding in Neuro-2A tumors. A region with high intensity of APT signal in the tumor tissue was consistent with the bleeding region. APT imaging mainly reflects the concentration of mobile proteins and peptides, as well as the pH. These important factors may be biomarkers for the diagnosis, treatment decision, prognosis, and assessment of treatment response in various diseases. In a previous study of human brain tumors, there were more mobile macromolecular protons in the tumor tissue than in the normal white matter on MRS, and the amount of these protons increased with higher tumor grade [29]. It has been reported that intracellular pH is slightly

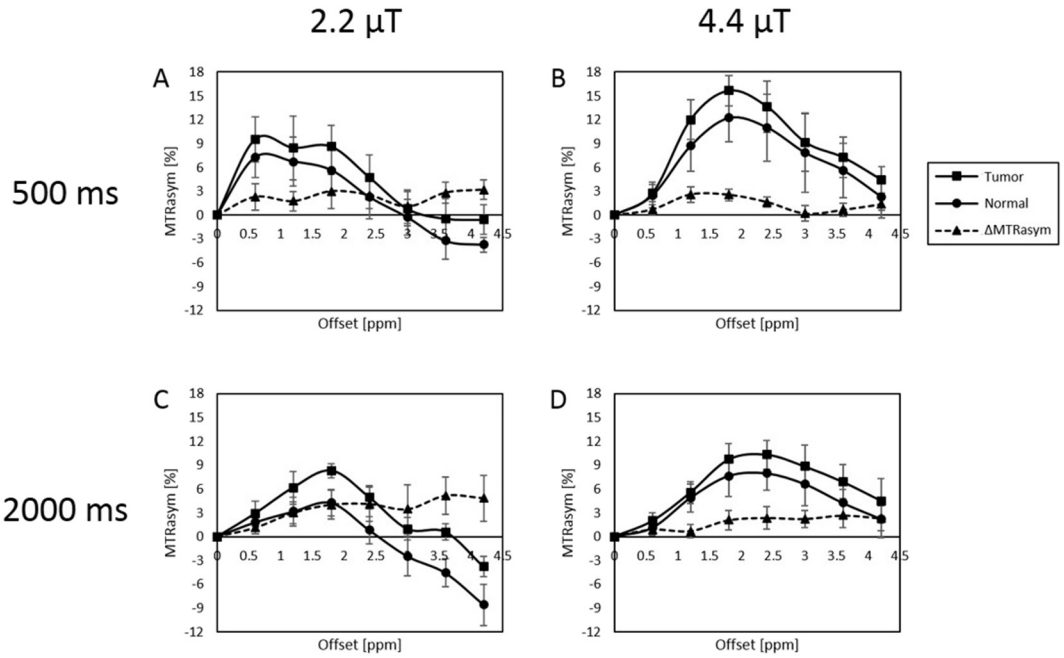

Fig. 5. Magnetization transfer ratio asymmetry (MTR_{asym}) of tumor and normal tissue and ΔMTR_{asym} between tumor and normal tissue. A: amplitude = 2.2 μT, pulse length = 500 ms. B: amplitude = 4.4 μT, pulse length = 500 ms. C: amplitude = 2.2 μT, pulse length = 2000 ms. D: amplitude = 4.4 μT, pulse length = 2000 ms.

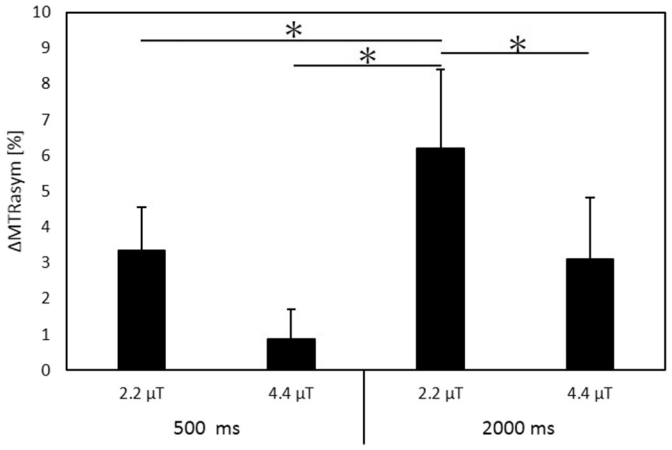

Fig. 6. Difference in magnetization transfer ratio asymmetry (ΔMTR_{asym}) at +3.6 ppm obtained at various conditions of saturation radio frequency pulse. ΔMTR_{asym} at an amplitude = 2.2 μT and pulse length = 2000 ms was significantly higher than that of the other conditions (*$p < 0.05$).

increased in tumors compared to normal brain tissue [30,31]. Hence, the APT signal of brain tumors is higher than that of normal brain tissue, and it increases with higher glioma grade [9,10]. In addition, it is known that the APT signal correlates with Ki-67-positive nuclei, and cell density indicative of active proliferation of tumor cells is associated with a high concentration of mobile peptides and proteins [10]. Therefore, the APT effect in brain tumors may reflect the proliferative potential of each tumor cell.

A relationship between APT signal and intracerebral hemorrhage (ICH) has been reported [13,32]. Hyperacute ICH caused by vessel rupture has high mobile protein content because it consists of red blood cells and white blood cells, among other cells. A high APT signal due to proteins such as hemoglobin has been observed in pure blood experiments [33]. Therefore, increased APT signal occurs in the region of ICH compared to normal brain tissue. Neuroblastoma is the most common extracranial solid tumor in childhood, and neuroblastic tumors are generally located in the abdomen [34]. Primary cerebral neuroblastomas, including an intraparenchymal calcified and cystic mass often with spontaneous hemorrhage and little edema, have been reported [35]. Our findings suggest that the APT effect in brain tumor reflects not only the proliferative potential of each tumor cell but also intratumoral bleeding.

4.2. Limitations

MTR asymmetry maps based on water protons at the offset frequency of the target molecule were used as CEST imaging signals. The MTR in the normal-appearing white matter show a negative value in APT maps [36]. Z-spectra include not only the APT signal but also the MT effect and NOE. Although MTR asymmetry eliminates direct saturation effects on water protons, it cannot eliminate the effect of MTC and NOE. Moreover, the increased semi-solid MT and the spill-over effects due to longer saturation pulses may diminish both APTR and native MTR asymmetry. Therefore, it is necessary to consider the negative MTR values affected by the NOE and spill-over effects. To address this problem, Z-spectral fitting methods, which correlate with the functions that correspond to APT, bulk water, MT effect, and NOE, should be used [37]. However, when using this method, it is necessary to prepare a more detailed Z-spectrum and to further investigate the imaging conditions in order to shorten the imaging time. In addition, although it was suggested that proliferative potential and bleeding are factors that contribute to increased APT signal, it is not clear which of the two factors affects the APT signal. Also, there are several factors in vivo that confound APT CEST imaging, including effects of tissue relaxation such as T_1 and T_2, semisolid MT, relayed NOE from aliphatic protons, and contributions from nearby exchanging protons such as amines. Moreover, CEST signals are influenced by various confounding effects, such as spill-over, MT and MT asymmetry, therefore the mechanism or degree of increased APT signal in tumors is difficult to determine [38].

APT CEST imaging is affected by tissue relaxation times such as T_1 and T_2. Furthermore, Zais et al. proposes that the use of apparent exchange-dependent relaxation (AREX) improves specificity of CEST as it is sensitive to the contents and the exchange rate of the APT pool without confounding effects like spillover, MT and T_1 relaxation [39].

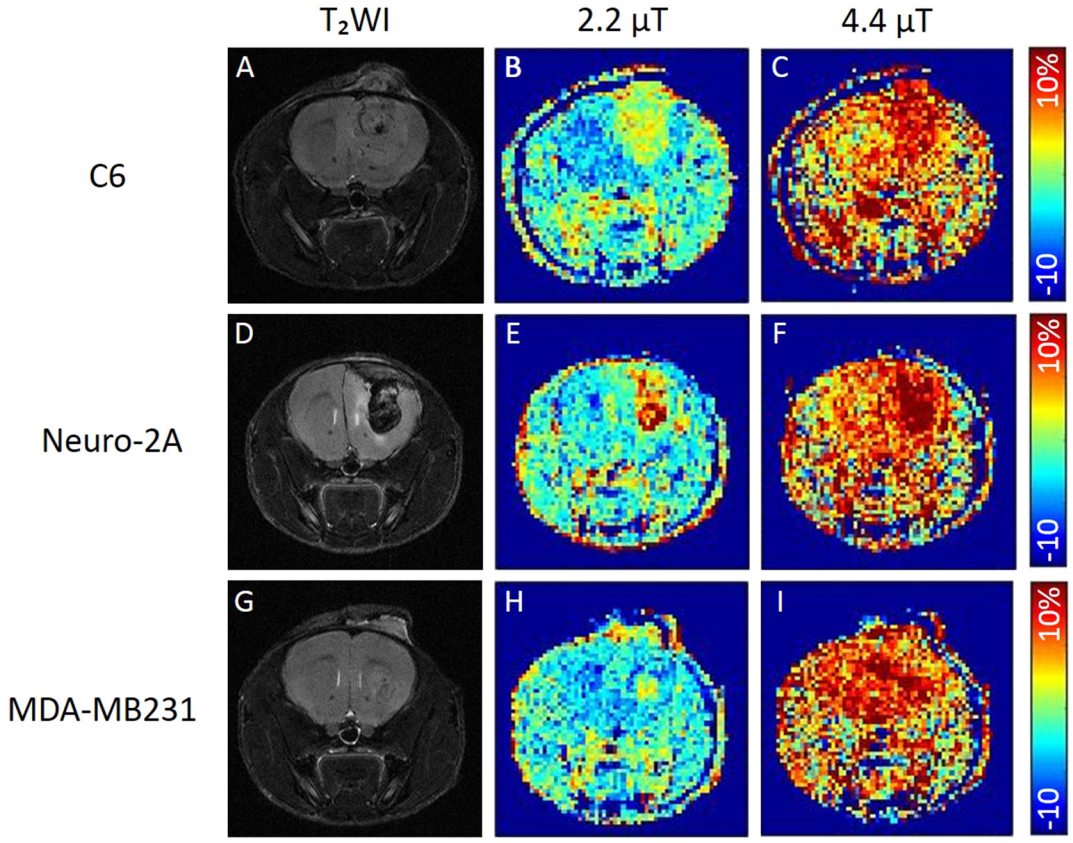

Fig. 7. Typical brain images of mouse tumors derived from C6 (A–C), Neuro-2A (D–F), and MDA-MB231 (G–I) cells. A, D, G: T_2-weighted images. Amide proton transfer (APT) images obtained with an amplitude of the saturation radio frequency pulse of 2.2 μT (B, E, H) or 4.4 μT (C, F, I).

Xu et al. has applied AREX as a method of correcting for R_1 relaxation in CEST imaging [38]. They reported that initially, the MTR and APT values were significantly higher in tumors; however, there was no significant difference in these parameters between the tumor tissue and the contralateral normal tissue after correcting the CEST values for R_1 relaxation using AREX [38]. The T_1 relaxation time reflects the proliferation and alteration of tumor cells according to previous studies [40,41]. In the present study, while we observed a significantly higher density of Ki-67-positive cells in the Neuro-2A tumors than in the C6 or MDA-MB231 tumors, it remains unclear whether the T_1 values differ between these three tumor types because we did not measure the T_1 values for each individual tumor cell. It is possible that the T_1 values of Neuro-2A tumors with bleeding may differ from those of the C6 and MDA-MB231 tumors. Our findings in this study showed that the MTR was significantly higher for the three tumors than for normal tissue, suggesting that APT imaging may be affected by the T_1 relaxation time in our study. Thus, measuring T_1 maps must be considered as a method of correcting for T_1 values when acquiring APT CEST images.

In MRI, B is a vector field that has magnitude and direction at each point in space. B is the combined magnetic field vector consisting of all the three types of magnetic field: the static field B0, the RF pulse B1, and the gradients. B0 inhomogeneity produces blurring, distortion, and

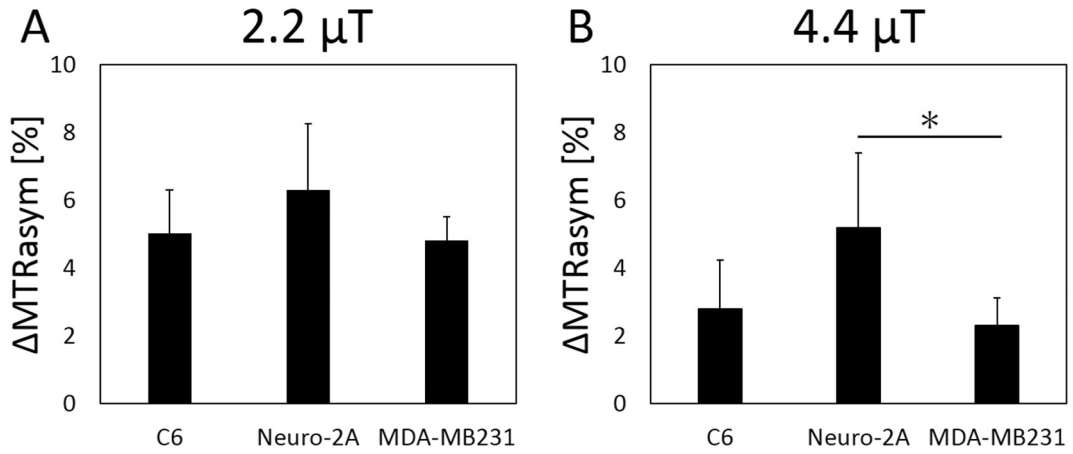

Fig. 8. Difference in magnetization transfer ratio asymmetry (ΔMTR_{asym}) at +3.6 ppm. (A) There was no difference in ΔMTR_{asym} between mouse models of brain tumors in images obtained at a pulse amplitude of 2.2 μT. (B) In images obtained at a pulse amplitude of 4.4 μT, ΔMTR_{asym} was significantly higher for Neuro-2A tumors than for MDA-MB231 tumors ($p < 0.05$).

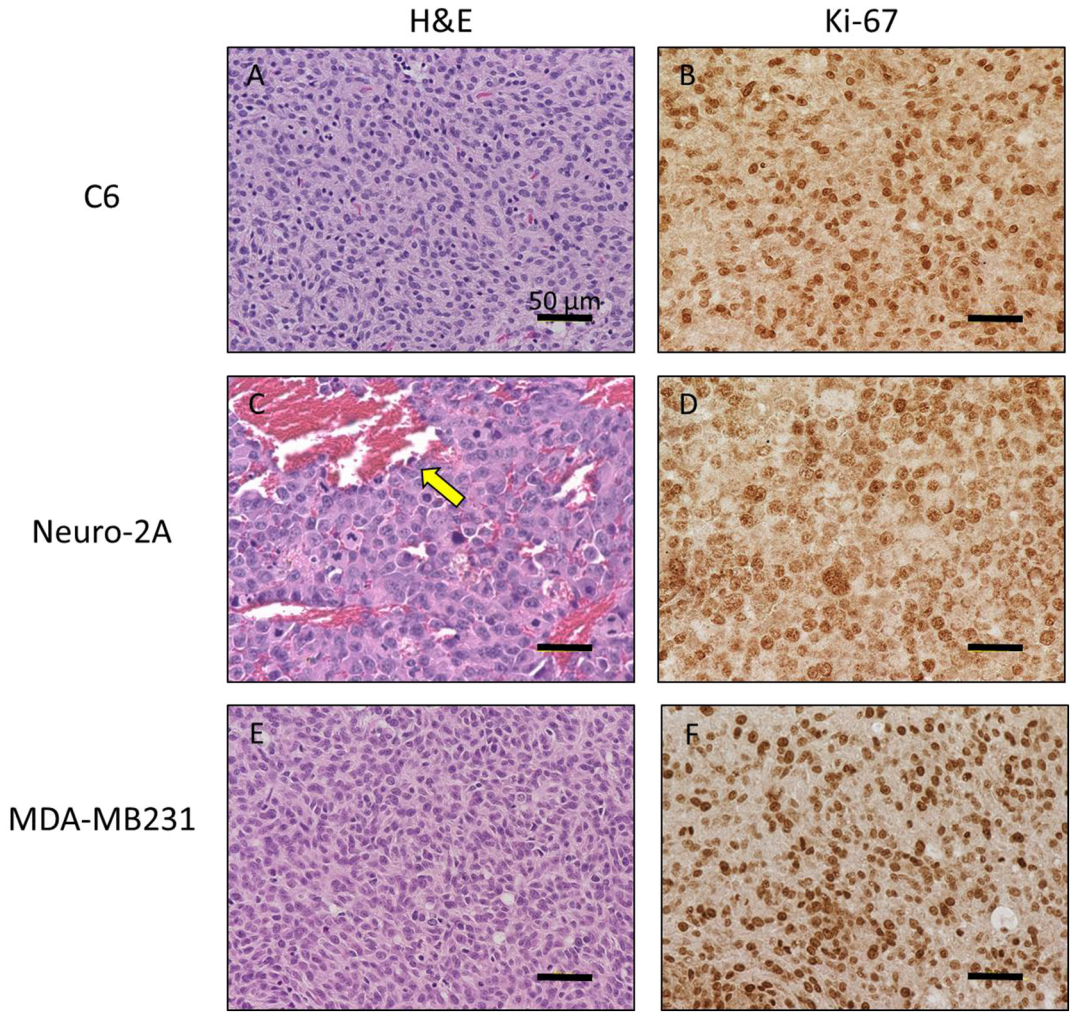

Fig. 9. Staining images of various tumor tissues (×400). (A, C, E) Hematoxylin and eosin (HE) staining. Intratumoral bleeding was observed in Neuro-2A tumors (yellow arrow). (B, D, F) Ki-67 immunohistochemical staining. Black bars equal 50 μm. (For interpretation of the references to colour in this figure, the reader is referred to the web version of this article.)

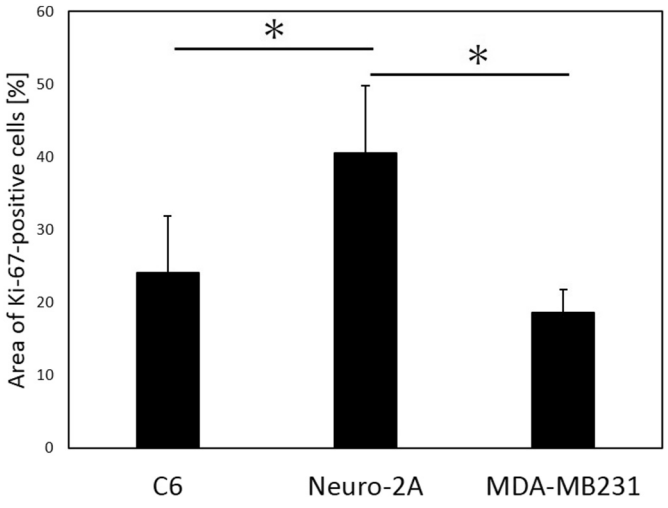

Fig. 10. Density of Ki-67-positive cells in different mouse brain tumors. The percentage of Ki-67-positive cells was significantly higher in Neuro-2A tumors than in C6 or MDA-MB231 tumors ($p < 0.05$).

signal loss at tissue interfaces. B1 inhomogeneity also leads to spatially-varying signal intensity of MR images. One of the technical difficulties of performing MRI at fields as high as 11.7 T is that the magnetic fields become inhomogeneous due to B0 and B1 [42]. In particular, CEST imaging is sensitive to the B0 and B1 fields, and field inhomogeneity persists despite recent advances in magnet technologies, especially for in vivo imaging at high fields [43]. Consequently, correction algorithms that can compensate for field inhomogeneity-induced measurement errors in CEST imaging may be useful. In fact, such a method is crucial for translating CEST imaging, where field inhomogeneity-induced artifacts can be corrected during post-processing, without prolonging the scan time. For example, Sun et al. demonstrated that the dependence of CEST contrast on the B0 field distribution may be addressed by developing a correction algorithm to compensate for the B0 field inhomogeneity-induced CEST imaging artifacts [44]. In our study, FAST-MAP algorithm was applied to correct for B0-field inhomogeneity in CEST imaging, but this was not enough. The water shift and B1 (WASABI) is a robust method of simultaneously mapping B0 and B1 within 1 min [45]. In future studies, one may consider applying these methods for B0 and B1 correction for CEST imaging.

4.3. Conclusion

MT pulse is an important parameter that should be adjusted depending on the target metabolite. We determined the suitable

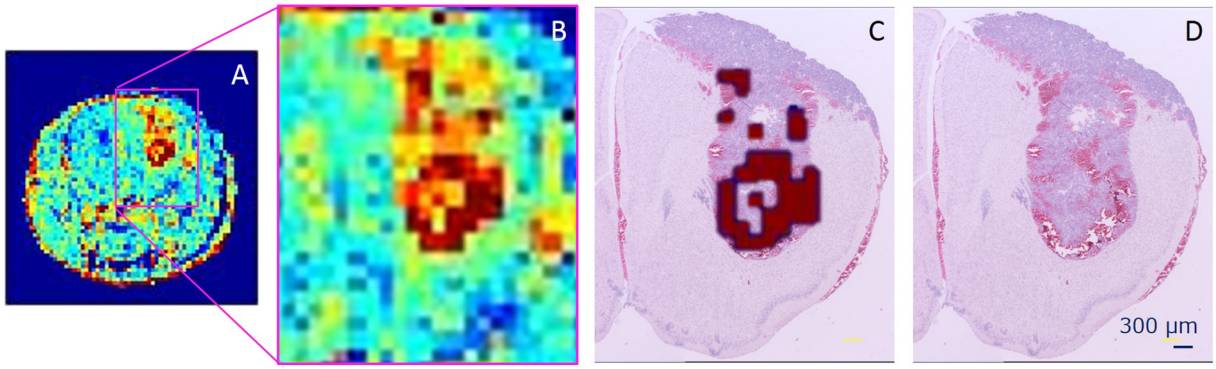

Fig. 11. APT maps of Neuro-2A model and HE staining (×20). The left image shows APT maps (A) and an enlarged view of one (B). The center image shows the region of high APT signal intensity (over the average intensity in tumor tissue) on HE staining (C). The right image shows HE staining (D). The region of intratumoral bleeding showed the highest APT signal intensity.

parameter of MT pulse for APT CEST imaging and used this technique to characterize tumors derived from orthotopic and ectopic tumor cells transplanted into the mouse brain. Noninvasive APT CEST imaging on an ultra-high-field MRI system was able to provide information about tumor characteristics, as confirmed by histological evaluation, such as tumor proliferation and bleeding.

Funding sources

This work was supported by Japan Society for the Promotion of Science (JSPS) KAKENHI [grant number 19K08172] and Japan Agency for Medical Research and Development (AMED) [grant number JP19dm0307026].

References

[1] Wu B, Warnock G, Zaiss M, Lin C, Chen M, Zhou Z, et al. An overview of CEST MRI for non-MR physicists. EJNMMI Phys 2016;3(1):19.
[2] Ward KM, Aletras AH, Balaban RS. A new class of contrast agents for MRI based on proton chemical exchange dependent saturation transfer (CEST). J Magn Reson 2000;143(1):79–87.
[3] Zhou J, Blakeley JO, Hua J, Kim M, Laterra J, Pomper MG, et al. Practical data acquisition method for human brain tumor amide proton transfer (APT) imaging. Magn Reson Med 2008;60(4):842–9.
[4] Saito S, Takahashi Y, Ohki A, Shintani Y, Higuchi T. Early detection of elevated lactate levels in a mitochondrial disease model using chemical exchange saturation transfer (CEST) and magnetic resonance spectroscopy (MRS) at 7T-MRI. Radiol Phys Technol 2019;12(1):46–54.
[5] Zaiss M, Bachert P. Chemical exchange saturation transfer (CEST) and MR Z-spectroscopy in vivo: a review of theoretical approaches and methods. Phys Med Biol 2013;58(22):R221–69.
[6] Louis DN, Perry A, Reifenberger G, von Deimling A, Figarella-Branger D, Cavenee WK, et al. The 2016 World Health Organization Classification of Tumors of the Central Nervous System: a summary. Acta Neuropathol 2016;131(6):803–20.
[7] Essig M, Anzalone N, Combs SE, Dorfler A, Lee SK, Picozzi P, et al. MR imaging of neoplastic central nervous system lesions: review and recommendations for current practice. AJNR Am J Neuroradiol 2012;33(5):803–17.
[8] Usinskiene J, Ulyte A, Bjornerud A, Venius J, Katsaros VK, Rynkeviciene R, et al. Optimal differentiation of high- and low-grade glioma and metastasis: a meta-analysis of perfusion, diffusion, and spectroscopy metrics. Neuroradiology 2016;58(4):339–50.
[9] Zhou J, Lal B, Wilson DA, Laterra J, van Zijl PC. Amide proton transfer (APT) contrast for imaging of brain tumors. Magn Reson Med 2003;50(6):1120–6.
[10] Togao O, Yoshiura T, Keupp J, Hiwatashi A, Yamashita K, Kikuchi K, et al. Amide proton transfer imaging of adult diffuse gliomas: correlation with histopathological grades. Neuro Oncol 2014;16(3):441–8.
[11] Togao O, Hiwatashi A, Yamashita K, Kikuchi K, Keupp J, Yoshimoto K, et al. Grading diffuse gliomas without intense contrast enhancement by amide proton transfer MR imaging: comparisons with diffusion- and perfusion-weighted imaging. Eur Radiol 2017;27(2):578–88.
[12] Zhou J, Payen JF, Wilson DA, Traystman RJ, van Zijl PC. Using the amide proton signals of intracellular proteins and peptides to detect pH effects in MRI. Nat Med 2003;9(8):1085–90.
[13] Ma X, Bai Y, Lin Y, Hong X, Liu T, Ma L, et al. Amide proton transfer magnetic resonance imaging in detecting intracranial hemorrhage at different stages: a comparative study with susceptibility weighted imaging. Sci Rep 2017;7:45696.
[14] Zhou J, Tryggestad E, Wen Z, Lal B, Zhou T, Grossman R, et al. Differentiation between glioma and radiation necrosis using molecular magnetic resonance imaging of endogenous proteins and peptides. Nat Med 2011;17(1):130–4.
[15] Salhotra A, Lal B, Laterra J, Sun PZ, van Zijl PC, Zhou J. Amide proton transfer imaging of 9L gliosarcoma and human glioblastoma xenografts. NMR Biomed 2008;21(5):489–97.
[16] Dowell NG, Tofts PS. Fast, accurate, and precise mapping of the RF field in vivo using the 180 degrees signal null. Magn Reson Med 2007;58(3):622–30.
[17] Kim M, Gillen J, Landman BA, Zhou J, van Zijl PC. Water saturation shift referencing (WASSR) for chemical exchange saturation transfer (CEST) experiments. Magn Reson Med 2009;61(6):1441–50.
[18] Zhao X, Wen Z, Huang F, Lu S, Wang X, Hu S, et al. Saturation power dependence of amide proton transfer image contrasts in human brain tumors and strokes at 3 T. Magn Reson Med 2011;66(4):1033–41.
[19] Zaiss M, Windschuh J, Goerke S, Paech D, Meissner JE, Burth S, et al. Downfield-NOE-suppressed amide-CEST-MRI at 7 Tesla provides a unique contrast in human glioblastoma. Magn Reson Med 2017;77(1):196–208.
[20] Saito S, Hasegawa S, Sekita A, Bakalova R, Furukawa T, Murase K, et al. Manganese-enhanced MRI reveals early-phase radiation-induced cell alterations in vivo. Cancer Res 2013;73(11):3216–24.
[21] Wada T, Togao O, Tokunaga C, Funatsu R, Kobayashi K, Nakamura Y. Effect of the saturation pulse duration on chemical exchange saturation transfer in amide proton transfer MR imaging: a phantom study. Radiol Phys Technol 2016;9(1):15–21.
[22] Togao O, Hiwatashi A, Keupp J, Yamashita K, Kikuchi K, Yoshiura T, et al. Amide proton transfer imaging of diffuse gliomas: effect of saturation pulse length in parallel transmission-based technique. PLoS One 2016;11(5):e0155925.
[23] Sun PZ, van Zijl PC, Zhou J. Optimization of the irradiation power in chemical exchange dependent saturation transfer experiments. J Magn Reson 2005;175(2):193–200.
[24] Zhou J, Hong X, Zhao X, Gao JH, Yuan J. APT-weighted and NOE-weighted image contrasts in glioma with different RF saturation powers based on magnetization transfer ratio asymmetry analyses. Magn Reson Med 2013;70(2):320–7.
[25] Tang X, Dai Z, Xiao G, Yan G, Shen Z, Zhang T, et al. Nuclear Overhauser enhancement-mediated magnetization transfer imaging in glioma with different progression at 7 T. ACS Chem Nerosci 2017;8(1):60–6.
[26] Cai K, Tain RW, Zhou XJ, Damen FC, Scotti AM, Hariharan H, et al. Creatine CEST MRI for differentiating gliomas with different degrees of aggressiveness. Mol Imaging Biol 2017;19(2):225–32.
[27] Cohen M, Jr. Ectopic pairing and evolution of 5S ribosomal RNA genes in the chromosomes of Drosophila funebris. Chromosoma 1976;55(4):349–57.
[28] Tremblay RG, Sikorska M, Sandhu JK, Lanthier P, Ribecco-Lutkiewicz M, Bani-Yaghoub M. Differentiation of mouse Neuro 2A cells into dopamine neurons. J Neurosci Methods 2010;186(1):60–7.
[29] Howe FA, Barton SJ, Cudlip SA, Stubbs M, Saunders DE, Murphy M, et al. Metabolic profiles of human brain tumors using quantitative in vivo 1H magnetic resonance spectroscopy. Magn Reson Med 2003;49(2):223–32.
[30] Griffiths JR. Are cancer cells acidic? Br J Cancer 1991;64(3):425–7.
[31] Ferrauto G, Di Gregorio E, Auboiroux V, Petit M, Berger F, Aime S, et al. CEST-MRI for glioma pH quantification in mouse model: validation by immunohistochemistry. NMR Biomed 2018;31(11):e4005.
[32] Wang M, Hong X, Chang CF, Li Q, Ma B, Zhang H, et al. Simultaneous detection and separation of hyperacute intracerebral hemorrhage and cerebral ischemia using amide proton transfer MRI. Magn Reson Med 2015;74(1):42–50.
[33] Zheng S, van der Bom IM, Zu Z, Lin G, Zhao Y, Gounis MJ. Chemical exchange saturation transfer effect in blood. Magn Reson Med 2014;71(3):1082–92.
[34] Ahmed AA, Zhang L, Reddivalla N, Hetherington M. Neuroblastoma in children: update on clinicopathologic and genetic prognostic factors. Pediatr Hematol Oncol 2017;34(3):165–85.
[35] Davis PC, Wichman RD, Takei Y, Hoffman JC, Jr. Primary cerebral neuroblastoma: CT and MR findings in 12 cases. AJR Am J Roentgenol 1990;154(4):831–6.
[36] Sagiyama K, Mashimo T, Togao O, Vemireddy V, Hatanpaa KJ, Maher EA, et al. In vivo chemical exchange saturation transfer imaging allows early detection of a therapeutic response in glioblastoma. Proc Natl Acad Sci U S A 2014;111(12):4542–7.
[37] Cai K, Singh A, Poptani H, Li W, Yang S, Lu Y, et al. CEST signal at 2ppm (CEST@

2ppm) from Z-spectral fitting correlates with creatine distribution in brain tumor. NMR Biomed 2015;28(1):1–8.
[38] Xu J, Zaiss M, Zu Z, Li H, Xie J, Gochberg DF, et al. On the origins of chemical exchange saturation transfer (CEST) contrast in tumors at 9.4 T. NMR Biomed 2014;27(4):406–16.
[39] Zaiss M, Bachert P. Exchange-dependent relaxation in the rotating frame for slow and intermediate exchange—modeling off-resonant spin-lock and chemical exchange saturation transfer. NMR Biomed 2013;26(5):507–18.
[40] Weidensteiner C, Allegrini PR, Sticker-Jantscheff M, Romanet V, Ferretti S, McSheehy PM. Tumour T1 changes in vivo are highly predictive of response to chemotherapy and reflect the number of viable tumour cells—a preclinical MR study in mice. BMC Cancer 2014;14:88.
[41] McSheehy PM, Weidensteiner C, Cannet C, Ferretti S, Laurent D, Ruetz S, et al. Quantified tumor t1 is a generic early-response imaging biomarker for chemotherapy reflecting cell viability. Clin Cancer Res 2010;16(1):212–25.
[42] Chen Z, Li SS, Yang J, Letizia D, Shen J. Measurement and automatic correction of high-order B0 inhomogeneity in the rat brain at 11.7 Tesla. Magn Reson Imaging 2004;22(6):835–42.
[43] Liu G, Song X, Chan KW, McMahon MT. Nuts and bolts of chemical exchange saturation transfer MRI. NMR Biomed 2013;26(7):810–28.
[44] Sun PZ, Farrar CT, Sorensen AG. Correction for artifacts induced by B(0) and B(1) field inhomogeneities in pH-sensitive chemical exchange saturation transfer (CEST) imaging. Magn Reson Med 2007;58(6):1207–15.
[45] Schuenke P, Windschuh J, Roeloffs V, Ladd ME, Bachert P, Zaiss M. Simultaneous mapping of water shift and B1 (WASABI)-application to field-inhomogeneity correction of CEST MRI data. Magn Reson Med 2017;77(2):571–80.